

Focusing Bistatic SAR Data in Airborne/Stationary Configuration

Robert Wang, *Member, IEEE*, Otmar Loffeld, *Senior Member, IEEE*, Yew Lam Neo, *Member, IEEE*, Holger Nies, Ingo Walterscheid, *Member, IEEE*, Thomas Espeter, *Member, IEEE*, Jens Klare, *Member, IEEE*, and Joachim H. G. Ender, *Senior Member, IEEE*

Abstract—This paper presents a frequency-domain based focusing algorithm for the bistatic SAR data in airborne/stationary configuration. In this bistatic configuration, only the moving platform contributes to the azimuth modulation, whereas the stationary platform introduces a range offset to the range migration trajectories of targets at the same range. The offset is determined by the azimuth position of different targets with respect to the stationary platform. Since the range offset is position-dependent, monostatic SAR imaging algorithms are not able to focus the bistatic data collected in this configuration. In this paper, an analytical bistatic point target reference spectrum is derived, and following that a frequency-domain based algorithm is developed to focus the bistatic data. It uses an interpolation-free Wavenumber Domain Algorithm (WDA) as a basis, and performs a range-variant interpolation to correct the position-dependent range offset in the image domain after coarse focusing. The proposed algorithm is validated by the simulated data and the real bistatic SAR data acquired by FGAN's airborne SAR system, PAMIR, in December 2007. In this bistatic SAR experiment, an X-band transmitter was stationary operated on a hill with PAMIR as the receiver mounted on a Transall C-160.

Index Terms—Bistatic Synthetic Aperture Radar (BiSAR), range cell migration (RCM), range offset (RO), wavenumber domain algorithm (WDA).

I. INTRODUCTION

BISTATIC Synthetic Aperture Radar (BiSAR) is characterized by different locations for transmitter and receiver and hence offers considerable capability, reliability and flexibility in designing BiSAR missions [1]–[3]. The bistatic configuration also brings additional benefits when compared to a monostatic SAR system like: frequent monitoring, resolution enhancement, reduced vulnerability for military applications, reduced costs using existing illuminators

of opportunity with several receive-only systems and also the possibility of forward- or backward-looking SAR imaging [3]–[6]. Bistatic systems with stationary illuminators (transmitters) appear interesting in this context, as they allow small and lightweight receive-only UAVs (Unmanned Aerial Vehicles) to produce bistatic SAR images [5]–[6].

Deriving the point target reference spectrum is a key step for frequency-domain based BiSAR processing. In the monostatic case, the Point Target Reference Spectrum (PTRS) is readily obtained by applying the Principle of Stationary Phase [7]–[8]. Furthermore, the RCM is azimuth-invariant, and hence targets located at the same slant ranges of closest approach will show identical migration trajectories in the range Doppler domain [7]. Point targets at differing azimuth locations will map into different (spotlight mode) or same (stripmap mode) segments of the identical arc. Many frequency-domain based monostatic algorithms make use of this property to achieve efficiency.

For the general bistatic configuration, there is no simple analytical solution due to existence of two independent hyperbolic range equations [2], [9]. For the airborne/stationary configuration, the stationary platform does not contribute to the azimuth modulation, and thus only a hyperbolic range equation for the moving platform is present, giving an analytical derivation of the PTRS. Although the stationary platform facilitates the derivation of the PTRS, it introduces a Coordinate-Dependent Range Offset (CDRO). Since one of the platforms is stationary, targets at the same range have the same Doppler history and the same RCM. However, the distance of these targets from the stationary platform varies in a hyperbolic form in azimuth due to their difference in azimuth position (see Fig. 1a), so the variation will result in the fact that the range migration trajectories of targets at the same range are distributed along a hyperbola [10], shown in Fig. 1b. Hence, they cannot be processed directly in the range-Doppler or 2-D frequency domain.

In [10], a Non-Linear Chirp Scaling (NLCS) algorithm is proposed, which can be shown to be suitable to process bistatic SAR data in airborne/stationary bistatic configuration. It circumvents the limitation of the coordinate-dependent RO by first correcting the linear RCM in the azimuth time domain, and then it uses a nonlinear perturbation function to equalize the targets' azimuth FM rates at the same range bins.

Manuscript received December 22, 2008; revised March 19, 2009 and May 29, 2009. This work was supported by the Germany Science Foundation under Grant Lo 455/7-1 BiFocus.

R. Wang, O. Loffeld, and H. Nies are with the Center for Sensorsystems, University of Siegen, 57076 Siegen, Germany (e-mail: wang@zess.uni-siegen.de).

Y. L. Neo is with the DSO National Labs, Singapore 118230.

I. Walterscheid, T. Espeter, J. Klare, and J. H. G. Ender are with the Research Institute for High Frequency Physics and Radar Techniques (FHR), Forschungsgesellschaft für Angewandte Naturwissenschaften (FGAN), 53343 Wachtberg, Germany.

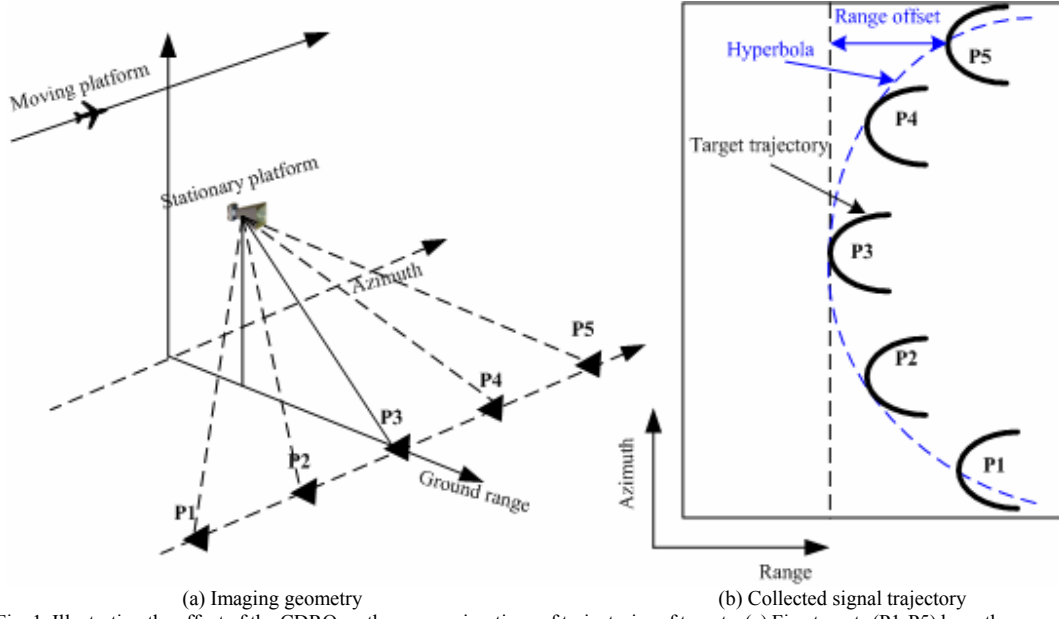


Fig. 1. Illustrating the effect of the CDRO on the range migrations of trajectories of targets. (a) Five targets (P1-P5) have the same range of closest approach from the moving platform. (b) The range migration trajectories (see the solid bold line) of the five targets are distributed along a hyperbola (see the dashed line). The range cell migration is exaggerated for purposes of clarity.

Subsequently, a single azimuth matched filtering can be applied at each range bin to compress the entire azimuth signal. Finally, an interpolation operation is applied to correct the misregistration due to the coordinate-dependent migration. In [11], a subaperture range-Doppler algorithm is used to process the bistatic SAR signal with a fixed receiver. Reference [12] presents a hybrid processing method for the fixed-receiver bistatic configuration.

This paper presents an analytical PTRS for airborne/stationary bistatic configurations. Based on the spectrum, a frequency-domain approach is developed. Firstly, it performs a Reference Function Multiplication (RFM) [7] to compress the range signal and to correct the bulk RCM. Secondly, an azimuth coarse focusing and a secondary RCMC are executed by using RFM in segmented range blocks. In each range block, nominal slant range parameters are used. This means that in these blocks the range variant components of the smaller differential RCM, the secondary range compression, and azimuth modulation are neglected [7]. In the coarse image domain, we perform the Coordinate-Dependent Range Offset Correction (CDROC) along the range direction using interpolation. The key idea of this correction is to migrate the targets along the hyperbola so that all targets having the same Doppler history are aligned in the same range bin. The alignment is performed via a range interpolation in the 2-D time domain on partially compressed targets, because in this domain targets are separated. Subsequently, the residual azimuth compression (to achieve proper compression) is easily done via fast convolution since all these targets in the same range cell experience the same residual modulation. After correcting the CDRO, we perform the Third Azimuth Compression (TAC) to compensate the residual phase.

This paper is organized as follows. In section II, the signal

model is presented and the PTRS is derived. Using this PTRS, a frequency-domain based focusing algorithm is developed in section III. We show the processing results of the simulated data in section IV and real bistatic SAR data in section V. Finally, some conclusions are reported in section VI.

NOMENCLATURE

τ, t	Azimuth and range time variables (Assume the azimuth time origin $\tau = 0$ to be the time of the closest approach from receiver to transmitter);
τ_{0R}	Zero Doppler time of receiver relative to the azimuth time origin $\tau = 0$;
r_{0R}	Slant range of receiver at zero Doppler time;
r_{0T}	Slant range of closest approach of target to a virtual transmitter path which is assumed parallel to the receiver's trajectory;
(τ_{0R}, r_{0R})	Receiver-referenced coordinates, defined as the coordinates of the target space;
$\sigma(\tau_{0R}, r_{0R})$	Backscattering coefficient of the point target located at (τ_{0R}, r_{0R}) ;
v_R	Platform velocity of receiver;
v_g	Ground velocity of the receiver's antenna footprint;
c	Speed of light;
λ, f_0	Carrier wavelength and carrier frequency of the transmitted signal;
f, f_τ	Range and azimuth frequency variables;
L_s	Width of the composite scene in azimuth;
L_f	Length of flight path during data acquisition;
L	Azimuth antenna footprint of transmitter;

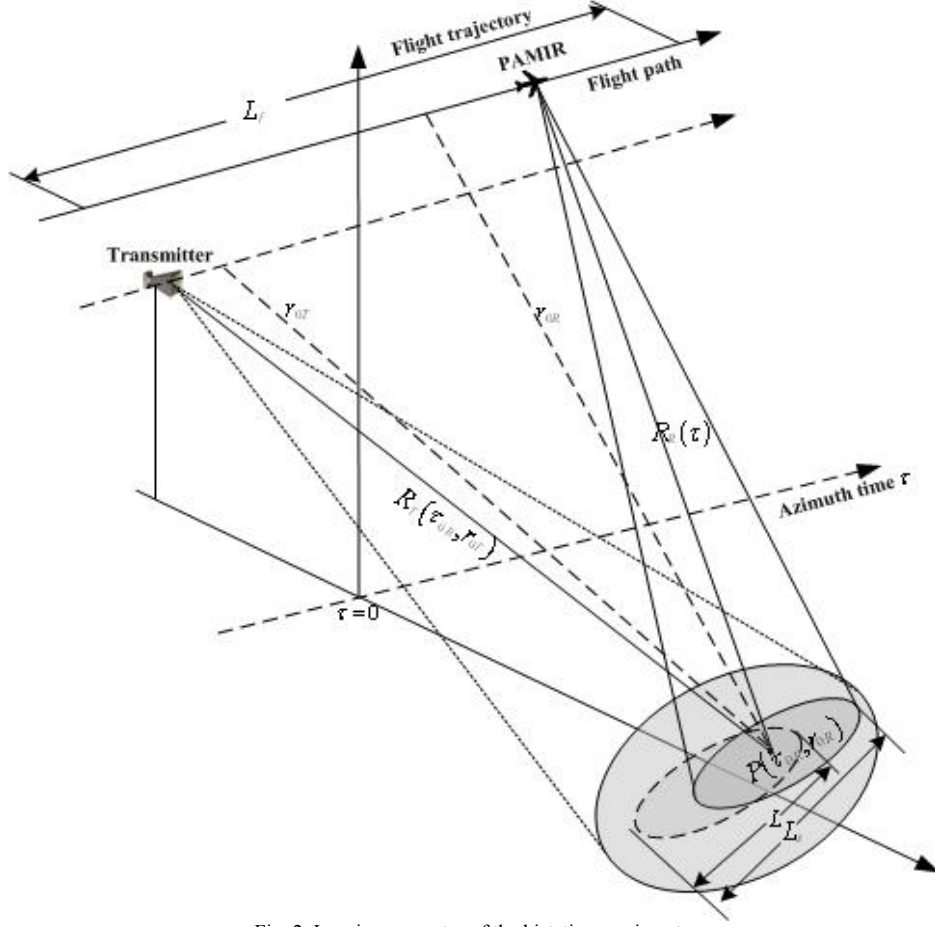


Fig. 2. Imaging geometry of the bistatic experiment

II. SIGNAL MODEL AND PTRS

We investigate airborne/stationary configurations, assuming a stationary transmitter as the illuminator and an airborne bistatic receiver mounted at an airplane. The receiver is operated in a sliding spotlight mode to achieve a tradeoff between the azimuth scene size and the azimuth resolution. The geometry is shown in Fig. 2.

The mathematical symbols and their definitions used in this paper are given in the nomenclature.

The received signal from a point target located at (τ_{0R}, r_{0R}) after demodulation is given by

$$g(\tau, t, \tau_{0R}, r_{0R}) = \text{rect}\left[\frac{\tau - \tilde{\kappa}\tau_{0R}}{L_e/v_R}\right] \text{rect}\left[\frac{\tau_{0R}}{L_s/v_R}\right] \sigma(\tau_{0R}, r_{0R}) \quad (1)$$

$$s_i\left[t - \frac{R_r(\tau) + R_T(\tau_{0R}, \tau_{0T})}{c}\right] \exp\left[-j2\pi \frac{R_r(\tau) + R_T(\tau_{0R}, \tau_{0T})}{\lambda}\right]$$

Where L_e is the synthetic aperture length, and given by $\kappa L + (1 - \kappa)L_f$. κ is a sliding factor, given by $\kappa = v_s/v_R$ [13]-[14]. $\tilde{\kappa}$ is the function of κ , and determines the working mode (see Table I). In (1), the first $\text{rect}[\bullet]$ represents the composite antenna pattern, simplified as a uniform illumination over the ground. The second rectangle function determines the extension of the illuminated area. $s_i(t)$ represents the

transmitted signal. $R_r(\tau)$ denotes the instantaneous slant range from the receiver to the point target, and $R_T(\tau_{0R}, r_{0T})$ is referred to the stationary slant range from the transmitter to the point target, they are given by

$$R_r(\tau) = \sqrt{r_{0R}^2 + v_R^2(\tau - \tau_{0R})^2} \quad (2)$$

$$R_T(\tau_{0R}, r_{0T}) = \sqrt{r_{0T}^2 + v_R^2\tau_{0R}^2} \quad (3)$$

Performing the Fourier Transform (FT) with respect to the fast time variable t , we can transform (1) into the range-frequency/azimuth-time domain.

$$G(\tau, f, \tau_{0R}, r_{0R}) = \text{rect}\left[\frac{\tau - \tilde{\kappa}\tau_{0R}}{L_e/v_R}\right] \text{rect}\left[\frac{\tau_{0R}}{L_s/v_R}\right] \sigma(\tau_{0R}, r_{0R}) \quad (4)$$

$$S_i(f) \exp\left[-j2\pi(f + f_0) \frac{R_r(\tau) + R_T(\tau_{0R}, \tau_{0T})}{c}\right]$$

where, $S_i(f)$ is the baseband spectrum of the transmitted signal.

It is important to note that the transmitter-related term in the exponential in (4) does not depend on the azimuth slow time τ , but only the (fixed) position of the point target. Applying azimuth FT, we obtain the PTRS in the two-dimensional frequency domain as

$$G(f_\tau, f, \tau_{0R}, r_{0R}) = \text{rect}\left[\frac{\tau_{0R}}{L_s/v_R}\right] \sigma(\tau_{0R}, r_{0R}) S_1(f) \times \exp\left[-j 2\pi(f + f_0) \frac{R_r(\tau_{0R}, r_{0R})}{c}\right] \times \int \text{rect}\left[\frac{\tau - \tilde{\kappa}\tau_{0R}}{L_e/v_R}\right] \exp[-j\phi_b(\tau, f_\tau)] d\tau \quad (5)$$

where, $\phi_b(\tau, f_\tau)$ is defined as

$$\phi_b(\tau, f_\tau) = 2\pi(f + f_0) \frac{R_r(\tau)}{c} + 2\pi f_\tau \tau \quad (6)$$

There is only one hyperbolic function of azimuth time in the integral of (5), instead of two independent hyperbolic range equations. This indicates that we only have a “semi-monostatic” phase history term. Therefore, the Principle of Stationary Phase can be readily applied to obtain the solution of the integral to derive the desired bistatic PTRS. At the point of stationary phase, the first derivative is zero

$$\left. \frac{d\phi_b(\tau, f)}{d\tau} \right|_{\tau=\tau_p} = 0 \quad (7)$$

Solving (7) for τ_p yields

$$\tau_p = \tau_{0R} - \frac{\frac{c r_{0R}}{v_R^2} f_\tau}{\sqrt{(f + f_0)^2 - \left(\frac{c f_\tau}{v_R}\right)^2}} \quad (8)$$

Substituting τ_p on the right-hand side of (5) for τ gives the desired PTRS,

$$G(f_\tau, f, \tau_{0R}, r_{0R}) = \text{rect}\left[\frac{f_\tau - f_{Dc}}{B_s}\right] \text{rect}\left[\frac{\tau_{0R}}{L_s/v_R}\right] \sigma(\tau_{0R}, r_{0R}) \times S_1(f) \exp[-j\Psi(f_\tau, f, \tau_{0R}, r_{0R})] \quad (9)$$

Where B_s denotes the bandwidth of a single point target, and given by $L_e v_R / (\lambda r_{0R})$. f_{Dc} represents the Doppler centroid, and formulated by $f_{Dc} = (1 - \tilde{\kappa}) v_R^2 \tau_{0R} / (\lambda r_{0R})$.

$$\Psi(f_\tau, f, \tau_{0R}, r_{0R}) = 2\pi(f + f_0) \frac{\sqrt{r_{0T}^2 + v_R^2 \tau_{0R}^2}}{c} + 2\pi \frac{r_{0R}}{c} \sqrt{(f + f_0)^2 - \left(\frac{c f_\tau}{v_R}\right)^2} + 2\pi f_\tau \tau_{0R} \quad (10)$$

Some short remarks concerning (9)-(10) will be helpful to understand the characteristics of this airborne/stationary configuration.

- The first windowing (rectangular) function of (9) shows the spectral characteristics in azimuth where the factor $\tilde{\kappa}$ determines the working mode of receiver. There are three major cases listed in Table I.
- The first term of (10) is a linear function of the range frequency, representing a range offset. Because of its square root factor, this range offset term is nonlinear in r_{0T} and τ_{0R} . It means that this offset term nonlinearly depends on the two-dimensional space coordinates of the illuminated target. Hence, it is called coordinate-dependent range offset. Because of this dependence, it cannot be completely corrected by chirp transformation approaches (e.g. chirp scaling [7] and inverse scaled Fourier

transformation [16]) in the range-Doppler or two-dimensional frequency domain, but has to be handled in the image domain. A proposed correction method will be discussed in section III.

- The second term of (10) is a semi-monostatic phase term contributed by the moving receiver. It contains a Doppler-dependent RCM term, which is well-known in monostatic SAR processing [7]. However, this Doppler-dependent term cannot be corrected independently by chirp transformations since chirp transformation may introduce a scaling factor into the first term of (10).

The overall azimuth signal bandwidth is obtained as the superposition of all the individual point target contributions, the maximum width for the azimuth frequency spectrum is obtained by determining the conditions for overlapping of the two rectangular windows $\text{rect}\left[\frac{f_\tau - (1 - \tilde{\kappa}) v_R^2 \tau_{0R} / (\lambda r_{0R})}{L_e v_R / \lambda r_{0R}}\right] \text{rect}\left[\frac{\tau_{0R}}{L_s / v_R}\right]$.

The azimuth frequency can be expressed as

$$|f_\tau| \leq \frac{\bar{B}_a}{2} = \frac{B_a}{2} + \frac{\Delta B_a}{2} \quad (11)$$

where \bar{B}_a indicates the bandwidth of the overall scene instead of the bandwidth of a single point target. ΔB_a represents an additional extension compared to the Doppler bandwidth of a single target and is given by

$$\Delta B_a = (1 - \tilde{\kappa}) \frac{v_R L_s}{\lambda r_{0R}} \quad (12)$$

From (12), we can see that the whole scene has a higher bandwidth compared with a single point target. To reduce the limitation of Pulse Repetition Frequency (PRF), we can upsample the azimuth data before azimuth focusing. In addition, this limitation can also be overcome by segmenting or dechirping in azimuth [17]-[18].

III. FOCUSING PROCEDURE

This section provides the processing steps of the proposed algorithm shown in Fig. 3 and illustrates its basic operation.

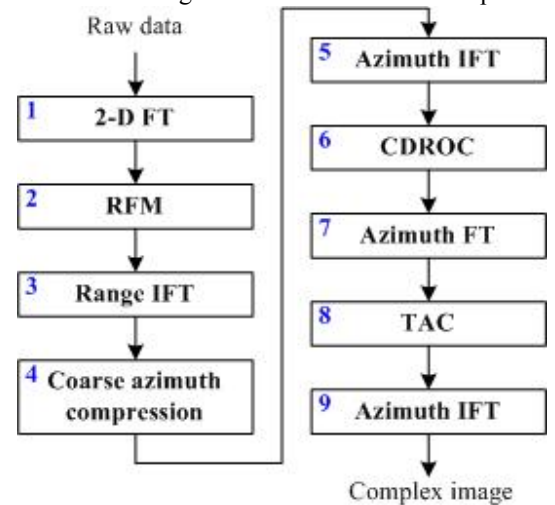
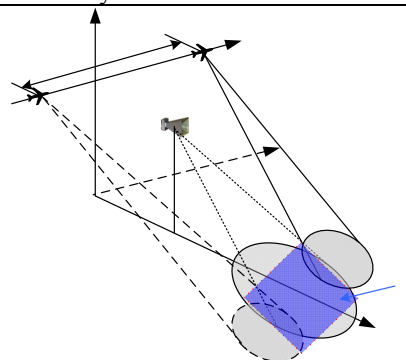
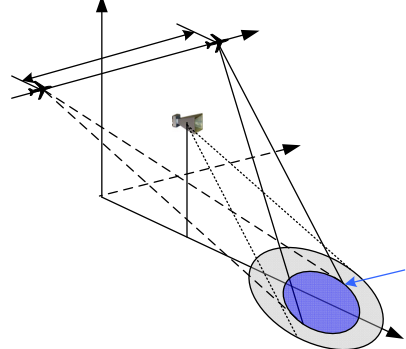
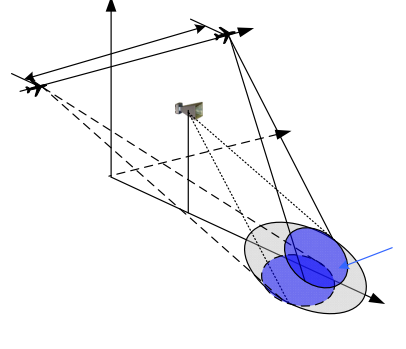


Fig. 3. Block diagram of the proposed focusing algorithm.

TABLE I
MODEL OF OPERATION AND GEOMETRY

$\tilde{\kappa}$	Mode	Description	Geometry
1	Stripmap ($v_g = v_R$)	The receiver works in the common stripmap mode where the azimuth signal has a bandwidth of $v_R L / (\lambda r_{0R})$	
0	Spotlight ($v_g = 0$)	The receiver operates in spotlight mode where the azimuth spectrum is centered around the frequency of $v_R^2 \tau_{0R} / (\lambda r_{0R})$. The bandwidth is given by $v_R L_f / (\lambda r_{0R})$ [14]-[15]. In this case, the antenna of receiver is steered around the rotation point, which is located at the center of the illuminated scene.	
$\frac{1}{\kappa}$	Sliding Spotlight ($0 < v_g < v_R$)	The receiver works in sliding spotlight mode [13] (also called stripmap/spotlight mode [14]-[15]). It is characterized by steering the beam around a virtual point, which is located beneath the earth's surface and far away from the scene center. In this case, the azimuth signal is centered on $(1 - \tilde{\kappa}) v_R^2 \tau_{0R} / (\lambda r_{0R})$, and has a bandwidth of $L v_R / (\lambda r_{0R})$. The azimuth bandwidth is increased by a factor $1/\kappa$ with respect to the stripmap case; in addition the azimuth size of the imaged scene is increased by a factor of $1 + \kappa(L_f/L)$ compared to the spotlight mode. Thus, this operational mode achieves a good tradeoff between the spotlight mode and the stripmap mode by steering the receiver's antenna. The sliding spotlight is a novel method as it does not really need the hardware of the radar to be more complex than the conventional spotlight mode. It tricks the radar into thinking that the spotlight mode has a scene center below the Earth's surface.	

The basic steps are outlined as follows:

1. Transform the raw data into the 2-D frequency domain.
2. Reference function multiplication (RFM). It is carried out to remove the space-invariant phase (i.e. perform bulk azimuth compression, bulk RCMC, range compression and bulk secondary range compression [7]). Thus, the RFM filter can be expressed as

$$H_{RFM}(f_a, f, R_m) = \exp\{j\Psi_{RFM}(f_\tau, f)\} \times S_i^*(f) \quad (13)$$

where $\Psi_{RFM}(f_\tau, f)$ is defined as

$$\Psi_{RFM}(f_\tau, f) = 2\pi \frac{R_m}{c} \sqrt{(f + f_0)^2 - \left(\frac{cf_\tau}{v_R}\right)^2} \quad (14)$$

R_m is a reference slant range, generally defined as the closest slant range from the scene center to the receiver. RFM filtering correctly focuses the data at the reference slant range, partially compensates the phases of targets at other ranges. After RFM filtering, the remaining phase in the two-dimensional frequency domain is

$$\begin{aligned}
\Psi_1(f_\tau, f, \tau_{0R}, r_{0R}) &= 2\pi(f + f_0) \frac{\sqrt{r_{0T}^2 + v_R^2 \tau_{0R}^2}}{c} \\
&+ 2\pi \frac{(r_{0R} - R_m)}{c} \sqrt{(f + f_0)^2 - \left(\frac{cf_\tau}{v_R}\right)^2} + 2\pi f_\tau \tau_{0R} \\
&\approx 2\pi(f + f_0) \frac{\sqrt{r_{0T}^2 + v_R^2 \tau_{0R}^2}}{c} \\
&+ 2\pi \frac{(r_{0R} - R_m)}{c} \left[f_0 D + \frac{f}{D} \right] + 2\pi f_\tau \tau_{0R}
\end{aligned} \quad (15)$$

Where D is the cosine of the instantaneous squint angle of the receiver [7], and formulated as $D = \sqrt{1 - (\lambda f_\tau / v_R)^2}$.

3. Perform IFT along the range direction to transform the signal into the range-Doppler domain. The resulting signal is given as

$$\begin{aligned}
G_1(f_\tau, t, \tau_{0R}, r_{0R}) &= \text{rect}\left[\frac{f_\tau - f_{Dc}}{B_a}\right] \text{rect}\left[\frac{\tau_{0R}}{L_s/v_R}\right] \sigma(\tau_{0R}, r_{0R}) \\
p_r\left(t - \frac{\sqrt{r_{0T}^2 + v_R^2 \tau_{0R}^2} + (r_{0R} - R_m)/D}{c}\right) &\exp[-j\Psi_2(f_\tau, \tau_{0R}, r_{0R})]
\end{aligned} \quad (16)$$

where $p_r(t)$ is the compressed pulse envelope in range;

$\Psi_2(f_\tau, \tau_{0R}, r_{0R})$ is given by

$$\Psi_2(f_\tau, \tau_{0R}, r_{0R}) = \frac{2\pi}{\lambda} \left[(r_{0R} - R_m)D + \sqrt{r_{0T}^2 + v_R^2 \tau_{0R}^2} \right] + 2\pi f_\tau \tau_{0R} \quad (17)$$

4. Focus the remaining azimuth signal coarsely. This step contains two functions: coarse azimuth compression and secondary RCMC. In this step, we first partition the data into range blocks in the slant range domain, and then transform every range block into the two-dimensional frequency domain by using the range FT. In every range block, we implement the RFM. The phase of the RFM filter is defined as

$$\Psi_{RFMn}(f_\tau, f, R_n) = 2\pi \frac{(R_n - R_m)}{c} \left[f_0 D + \frac{f}{D} \right] \quad (18)$$

where the subscript n represents the index of the range blocks across the whole swath. R_n is referred as to the reference slant range of the n^{th} block (usually the midswath range in the block). In every block, if we want to keep the azimuth broadening due to RCMC errors less than 2%, then we should keep the uncorrected RCM within half of a range resolution cell [7]. The target range migration trajectory is r_{0R}/D in the range Doppler domain, so that the RCM is $r_{0R}(1/D - 1)$ [7]. Hence, the constraint for the residual RCM in this step is given as

$$\left| (r_{0R} - R_n) \left[\frac{1}{D} - 1 \right] \right| \leq \frac{\delta_R}{2} \quad (19)$$

δ_R is the range resolution cell. Equation (19) can help us determine the block length in the slant range direction. After this coarse focusing, the RCMC errors can be disregarded, and thus, the signal in the range-Doppler domain is

$$\begin{aligned}
G_2(f_\tau, t, \tau_{0R}, r_{0R}) &= \text{rect}\left[\frac{f_\tau - f_{Dc}}{B_a}\right] \text{rect}\left[\frac{\tau_{0R}}{L_s/v_R}\right] \sigma(\tau_{0R}, r_{0R}) \\
p_r\left(t - \frac{\sqrt{r_{0T}^2 + v_R^2 \tau_{0R}^2} + (r_{0R} - R_n)}{c}\right) &\exp[-j\Psi_3(f_\tau, \tau_{0R}, r_{0R})]
\end{aligned} \quad (20)$$

$$\Psi_3(f_\tau, \tau_{0R}, r_{0R}) = \frac{2\pi}{\lambda} \left[(r_{0R} - R_n)D + \sqrt{r_{0T}^2 + v_R^2 \tau_{0R}^2} \right] + 2\pi f_\tau \tau_{0R} \quad (21)$$

From (20), it can be seen that the range signal is registered to the relative position of the reference slant range in the n^{th} block. Examining (21) suggests that the azimuth modulation has not been removed completely, the residual azimuth modulation is $2\pi(r_{0R} - R_n)D/\lambda$. It means that we have only achieved a coarse azimuth compression at this stage.

5. Perform an IFT in azimuth to transform the signal into the coarse image domain. The result is

$$\begin{aligned}
\tilde{g}_2(\tau, t, \tau_{0R}, r_{0R}) &= \int G_2(f_\tau, t, \tau_{0R}, r_{0R}) \exp(j2\pi f_\tau \tau) df_\tau \\
&= \text{rect}\left[\frac{\tau_{0R}}{L_s/v_R}\right] \sigma(\tau_{0R}, r_{0R}) p_r\left(t - \frac{\sqrt{r_{0T}^2 + v_R^2 \tau_{0R}^2} + (r_{0R} - R_n)}{c}\right) \\
&\exp\left[-j\frac{2\pi}{\lambda} \sqrt{r_{0T}^2 + v_R^2 \tau_{0R}^2}\right] \\
&\int \text{rect}\left[\frac{f_\tau - f_{Dc}}{B_a}\right] \exp\left\{-j\left[\frac{2\pi}{\lambda} (r_{0R} - R_n)D - 2\pi f_\tau (\tau - \tau_{0R})\right]\right\} df_\tau \\
&= \text{rect}\left[\frac{\tau_{0R}}{L_s/v_R}\right] \sigma(\tau_{0R}, r_{0R}) p_r\left(t - \frac{\sqrt{r_{0T}^2 + v_R^2 \tau_{0R}^2} + (r_{0R} - R_n)}{c}\right) \\
&\tilde{p}_a(\tau - \tau_{0R}) \exp\left[-j\frac{2\pi}{\lambda} \sqrt{r_{0T}^2 + v_R^2 \tau_{0R}^2}\right]
\end{aligned} \quad (22)$$

Since the residual azimuth modulation (i.e. $2\pi(r_{0R} - R_n)D/\lambda$) is present, the azimuth signal is coarsely focused. The coarse azimuth impulse response $\tilde{p}_a(\tau)$ is expressed as

$$\tilde{p}_a(\tau) = \int \text{rect}\left[\frac{f_\tau - f_{Dc}}{B_a}\right] \exp\left\{j\left[2\pi f_\tau \tau - \frac{2\pi}{\lambda} (r_{0R} - R_n)D\right]\right\} df_\tau \quad (23)$$

For clarity, its counterpart (i.e. the ideal azimuth impulse response) is given as

$$\begin{aligned}
\rho_a(\tau) &= \int \text{rect}\left[\frac{f_\tau - f_{Dc}}{B_a}\right] \exp[j2\pi f_\tau \tau] df_\tau \\
&= B_a \text{sinc}[B_a \tau] \exp[j2\pi f_{Dc} \tau]
\end{aligned} \quad (24)$$

Because the residual error exists over the short subswaths (i.e. narrow swath), it only results in the slight degradation. Therefore, this coarse azimuth compression can separate the targets in azimuth. Thus, this separation in azimuth is helpful to correct the dependency of the range offset on the azimuth coordinate of targets in the next step.

6. Correct the nonlinear coordinate-dependent range offset along the range direction. The correction maps the original nonlinear slant range into a linear one, that is.

$$\sqrt{r_{0T}^2 + v_R^2 \tau_{0R}^2} \rightarrow r_{0T} \quad (25)$$

To implement the mapping operation, a range-direction time-domain interpolator can be used (Generally, an 8-point

sinc interpolation kernel appears to be sufficient [7]). After this nonlinear correction, (22) becomes

$$\begin{aligned} \tilde{g}_3(\tau, t, \tau_{0R}, r_{0R}) &= \text{rect}\left[\frac{\tau_{0R}}{L_s/v_R}\right] \sigma(\tau_{0R}, r_{0R}) \tilde{p}_a(\tau - \tau_{0R}) \\ p_r\left(t - \frac{r_{0T} + (r_{0R} - R_n)}{c}\right) &\exp\left[-j\frac{2\pi}{\lambda}\sqrt{r_{0T}^2 + v_R^2\tau_{0R}^2}\right] \end{aligned} \quad (26)$$

Subsequently, the residual azimuth compression can be implemented by using matched filtering in the range-Doppler domain since all these targets in the same range cell hold the same residual modulation.

7. Transform the coarse image back into the range-Doppler domain to remove the residual azimuth modulation. Combining (23) and (26) yields

$$\begin{aligned} \tilde{G}_3(f_\tau, t, \tau_{0R}, r_{0R}) &= \text{rect}\left[\frac{\tau_{0R}}{L_s/v_R}\right] \sigma(\tau_{0R}, r_{0R}) p_r\left(t - \frac{r_{0T} + r_{0R} - R_n}{c}\right) \\ &\exp\left[-j\frac{2\pi}{\lambda}\sqrt{r_{0T}^2 + v_R^2\tau_{0R}^2}\right] \int \tilde{p}_a(\tau - \tau_{0R}) \exp(-j2\pi f_\tau \tau) d\tau \\ &= \text{rect}\left[\frac{\tau_{0R}}{L_s/v_R}\right] \text{rect}\left[\frac{f_\tau - f_{Dc}}{B_a}\right] \sigma(\tau_{0R}, r_{0R}) \\ &p_r\left(t - \frac{r_{0T} + (r_{0R} - R_n)}{c}\right) \exp[-j\Psi_3(f_\tau, \tau_{0R}, r_{0R})] \end{aligned} \quad (27)$$

8. Perform the Third Azimuth Compression (TAC) to remove the residual modulation term by using the range-variant matched filtering. The filter is defined as

$$H_a(f_\tau, r_{0R}, R_n) = \exp\left[j\frac{2\pi}{\lambda}(r_{0R} - R_n)D\right] \quad (28)$$

After TAC, the residual azimuth modulation is compensated and the remaining signal can be expressed as

$$\begin{aligned} G_3(f_\tau, t, \tau_{0R}, r_{0R}) &= \tilde{G}_3(f_\tau, t, \tau_{0R}, r_{0R}) \times H_a(f_\tau, r_{0R}, R_n) \\ &= \text{rect}\left[\frac{f_\tau - f_{Dc}}{B_a}\right] \text{rect}\left[\frac{\tau_{0R}}{L_s/v_R}\right] \sigma(\tau_{0R}, r_{0R}) \\ &p_r\left(t - \frac{r_{0T} + (r_{0R} - R_n)}{c}\right) \exp\left[-j\left(\frac{2\pi}{\lambda}\sqrt{r_{0T}^2 + v_R^2\tau_{0R}^2} + 2\pi f_\tau \tau_{0R}\right)\right] \end{aligned} \quad (29)$$

9. Transform the signal into the complex image domain by performing an IFT in azimuth. We obtain

$$\begin{aligned} g_3(\tau, t, \tau_{0R}, r_{0R}) &= \text{rect}\left[\frac{\tau_{0R}}{L_s/v_R}\right] \sigma(\tau_{0R}, r_{0R}) p_r\left(t - \frac{r_{0T} + (r_{0R} - R_n)}{c}\right) \\ &p_a(\tau - \tau_{0R}) \exp\left[-j\frac{2\pi}{\lambda}\sqrt{r_{0T}^2 + v_R^2\tau_{0R}^2}\right] \end{aligned} \quad (30)$$

The exponential term of (30) denotes a residual phase term which can be corrected by phase multiplication in the image domain. If a magnitude image is the final product, it can be negligible.

IV. SIMULATION EXPERIMENT

In this section, we perform a simulation experiment based on data collection geometry shown in Fig. 4(a).

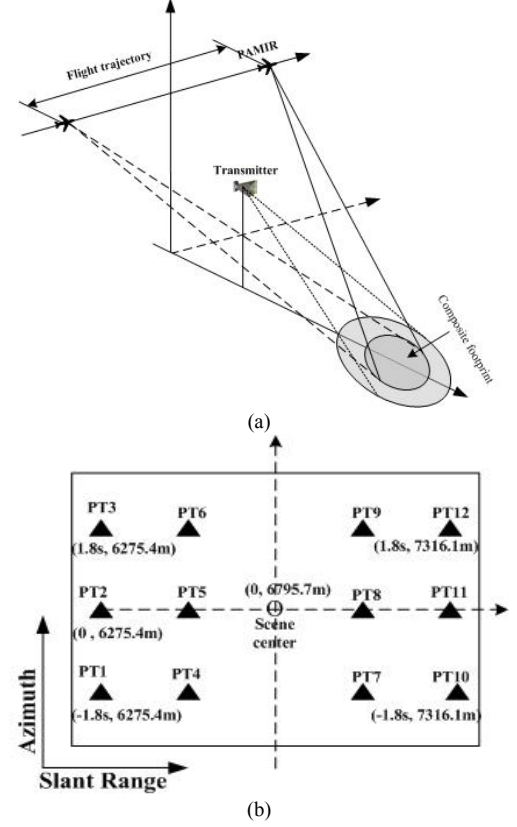


Fig. 4. Illustration of the geometry of simulation experiment. (a) Imaging geometry. (b) Composite scene with twelve point targets.

In this simulation, the receiver works in spotlight mode, that is, $\kappa = 0$. The simulated scene consists of twelve point targets, which are arranged in a rectangular pattern (i.e. a 3×4 matrix), shown in Fig. 4 (b). The coordinates of targets are referenced to the receiver, i.e. (τ_{0R}, r_{0R}) . The parameters are listed in Table II.

TABLE II
AIRBORNE/STATIONARY BISTATIC SAR SYSTEM PARAMETERS

	Receiver	Transmitter
Carrier frequency	9.65GHz	
Range bandwidth	380 MHz	
Sampling rate	494 MHz	
PRF	600 Hz	
Velocity	100m/s	0
Altitude	2872 m	94 m
Depression angle	25 °	5 °
Beam width	6.0°	20 °
Composite exposure time	5.12 s	

Since the moving receiver works in spotlight mode, the Doppler bandwidths of these targets are dependent on the slant range of receiver at zero Doppler time, i.e. r_{0R} . Using the parameters listed in Table II, the calculated Doppler bandwidths of the twelve targets are: 262.62 Hz (PT1-PT3), 255.56 Hz (PT4-PT6), 230.73 Hz (PT7-PT9), and 225.26 Hz

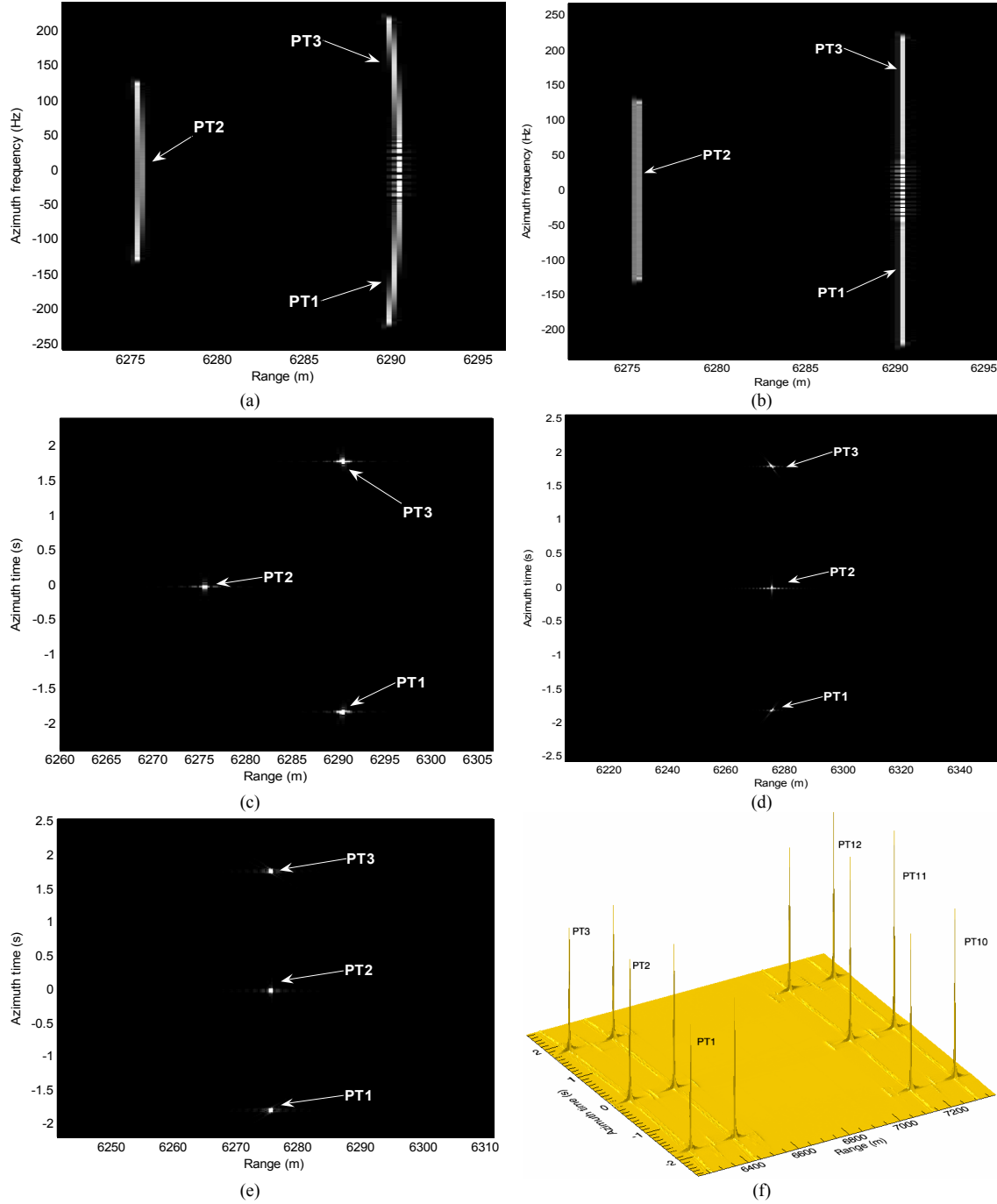


Fig. 5. Interpretation of the main processing steps (PT1-PT3 are used for explanation). (a) First RFM in the range-Doppler domain (Step 3). (b) Secondary RCMC in the segmented blocks (Step 4). (c) Coarse azimuth focusing (Step 4). (d) CDROC (Step 6). (e) Image after the third azimuth compression (Step 9). (f) Focused result of the simulated scene.

(PT10 - PT12). In this simulation, the maxima of the Doppler spectrum shift and Doppler bandwidth are ± 92.32 Hz and 262.62 Hz, respectively. So, for the simulated scene, the extension for azimuth frequency is less than ± 223.64 Hz. Thus, a PRF of 600 Hz can properly sample the azimuth signal. By using (19), the range block size is 298 samples, and the resulting number of range blocks is 14. In addition, it needs to be emphasized that a rectangular window is used in the range and azimuth processing.

A. Illustration of Processing Procedure

For clarity of the presented imaging algorithm, the effects of the RFM, coarse azimuth compression, CDROC, and TAC are illustrated in Fig. 5. For this illustration, we concentrate on PT1-PT3, which are the worst case for focusing, being furthest from the reference range.

In Fig. 5(a), the RCMs of PT1-PT3 have not been corrected accurately, since the RFM only corrects the RCM of

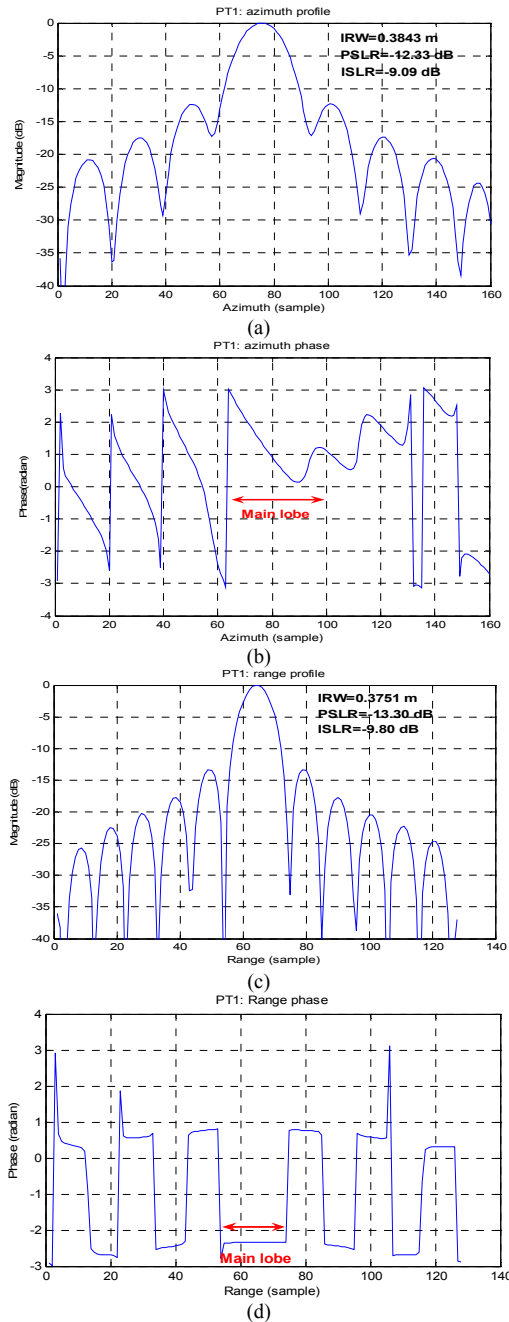
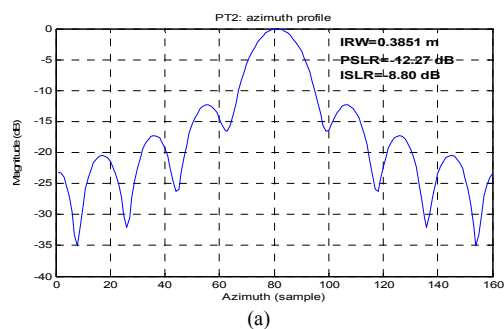
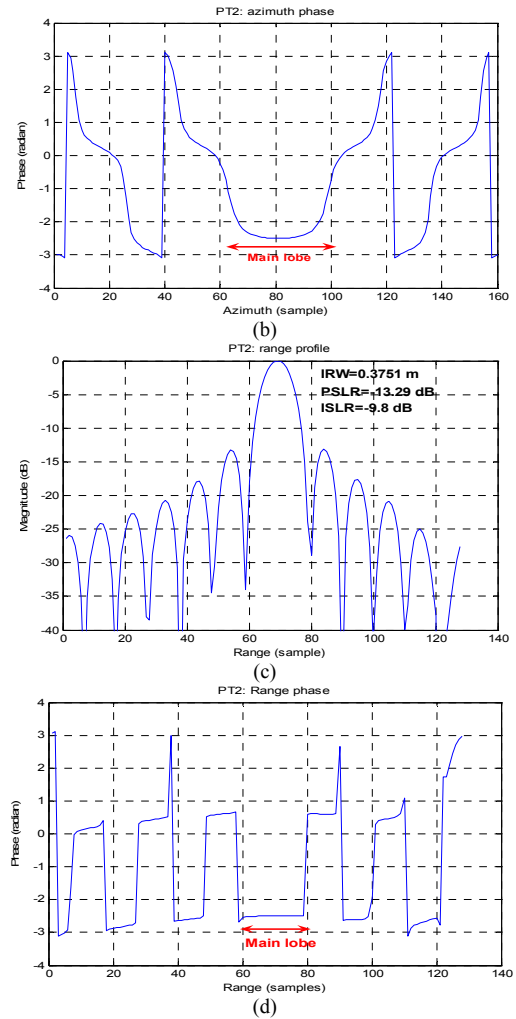


Fig. 6. Impulse responses and phases of PT1 in the coarse image domain. (a) Azimuth profile. (b) Azimuth phase. (c) Range profile. (d) Range phase.



(a)



(d)

Fig. 7. Impulse responses and phase of PT2 in the coarse image domain. (a) Azimuth profile. (b) Azimuth phase. (c) Range profile. (d) Range phase.

targets located near the reference range. For the targets away from the reference slant range, e.g. PT1-PT3, the RCM is only partially corrected. In addition, from Fig. 5(a), it also can be seen that PT1 and PT3 are in the same range bin to PT2 and are shifted to another range bin due to the dependence of $R_r(\tau_{0R}, \tau_{0T})$ on the azimuth coordinate. Figure 5(a) also shows that the PT1 and PT3 differ in Doppler centroid compared with PT2, which causes an extension of the Doppler spectrum of the whole scene. Furthermore, the trajectories of PT1 and PT3 also appear to be more considerable in RCM.

After the secondary RCMC, the RCM introduced by the moving platform is corrected under an acceptable level, as shown in Fig. 5(b). In Fig. 5(c), the coarsely focused image is shown. It is clear that PT1 and PT3 are migrated in range as a result of the CDRO. In Fig. 5(c), PT1 and PT3 are registered to (-1.8s, 6290.4 m) and (1.8s, 6290.4m), respectively. Subsequently, in step 6, the range-variant interpolation is used to correct the range offset. After this correction, PT1 and PT3 are registered to (-1.8s, 6275.4 m) and (1.8s, 6275.4m), shown in Fig. 5(d). It needs to be emphasized that 8-point sinc interpolation kernels are used for this interpolation operation. Fig. 5(e) gives the final image after TAC. The focusing result

of the whole simulated scene is shown in Fig. 5(f).

B. Focusing Quality

To quantify the precision of the presented processing method, PT1 and PT2 are analyzed in more detail (Since PT1 and PT3 are located symmetrically in azimuth, we only measure the quality parameters of PT1). The theoretical range resolution is 0.3758 m, and the azimuth resolution is 0.3808 m.

To check on the focusing quality of the coarse image (i.e. processing result of step 1-step 5 in Fig.3), the impulse responses and phases of PT1 and PT2 in both the range and azimuth directions are shown in Fig. 6 and Fig. 7, respectively.

Examining the azimuth quality parameters shown in the annotation of Fig. 6 (a) and Fig. 7 (a), it can be seen that the azimuth impulse responses of PT1 and PT2 suffer from the focusing degradation. This degradation as a result of the residual azimuth modulation can be illustrated in Fig. 6 (b) and Fig. 7(b), where the phases are curved by the residual azimuth modulation through the main lobe [7].

The measured range resolutions of PT1 and PT2 agree well with the theoretical value, shown in Fig. 6 (c) and Fig. 7 (c). The measured PSLR and ISLR deviate from the theoretical values of -13.26 dB and -9.72 dB by less than 0.2dB. Figs. 6 (d) and 7 (d) also show that the range phases of both targets are flat through the main lobe.

To compensate the residual azimuth modulation, steps 6-9 are applied, and the resulting impulse responses and phases of PT1 and PT2 are shown in Figs. 8 and Fig. 9, respectively.

As can be seen from Figs. 8 (a) and 9 (a), the azimuth focusing quality of PT1 and PT2 is improved after the residual azimuth compression. This improvement can also be explained by the azimuth phases shown in Figs. 8 (b) and 9 (b). Looking at the azimuth phase in Fig. 8 (b), it can be seen that the residual azimuth modulation presented in Fig. 6 (b) has been removed by TAC. And, the azimuth phase of PT1 appears to be a straight slope, which can be compared with Fig. 6 (b). The slope can be interpreted by the linear phase ramp in the last exponential term in (24) [7]. When the azimuth signal has the nonzero Doppler centroid (e.g. PT1, shown in Fig. 5 (a)), the phase is linear through the main lobe. In Fig. 9 (b), the azimuth phase of PT2 is flat within the main lobe after residual azimuth compression due to the fact that PT2 has the zero Doppler centroid (see Fig. 5 (a)).

Since the residual azimuth compression is implemented in azimuth, it has no effect on the range impulse response, which can be verified by Figs. 8 (c) and 9 (c). However, the residual azimuth compression can introduce a phase ramp into range phase. The range phase is caused by the fact that the azimuth residual matched filter FM rate changes with range, while all parts of a given target have a constant FM rate [7]. Therefore, the azimuth FM rate mismatch introduces a phase error which appears to be approximately linear in range, shown in Figs. 8 (d) and 9 (d) [7].

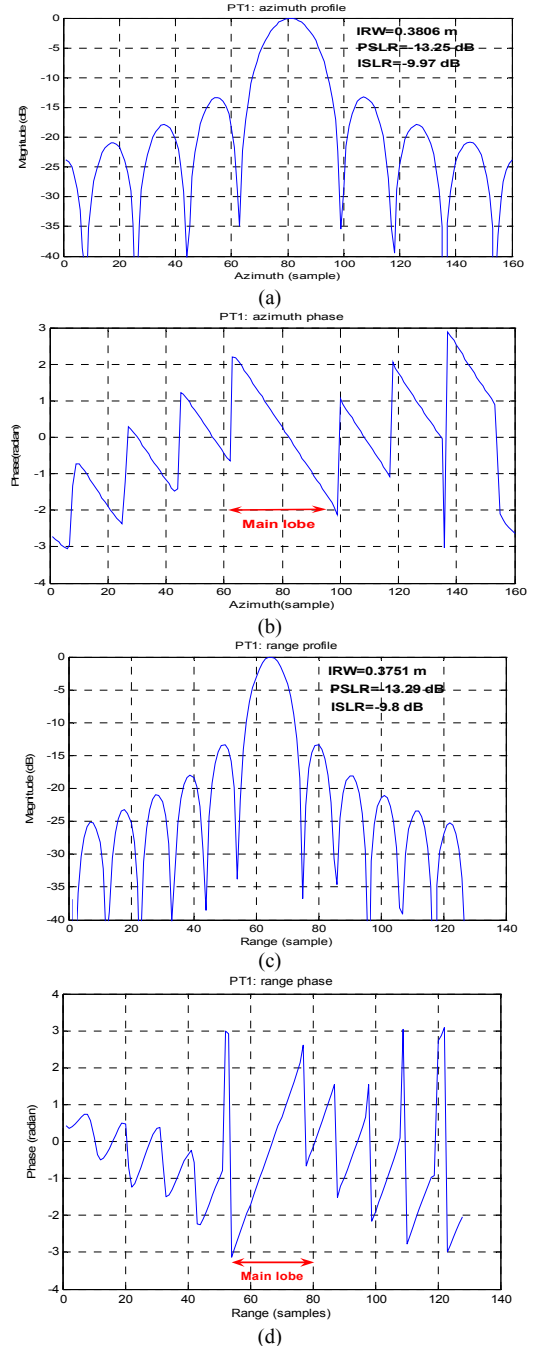
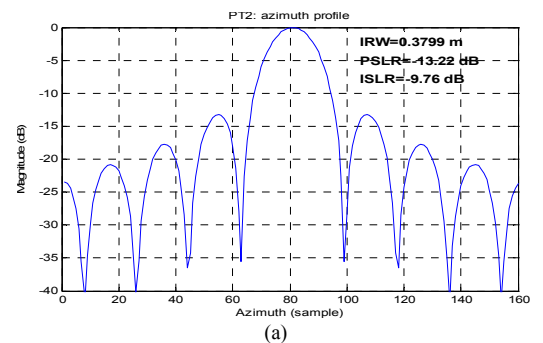


Fig. 8. Impulse responses and phases of PT1 after the compensation of residual phase. (a) Azimuth profile. (b) Azimuth phase. (c) Range profile. (d) Range phase.



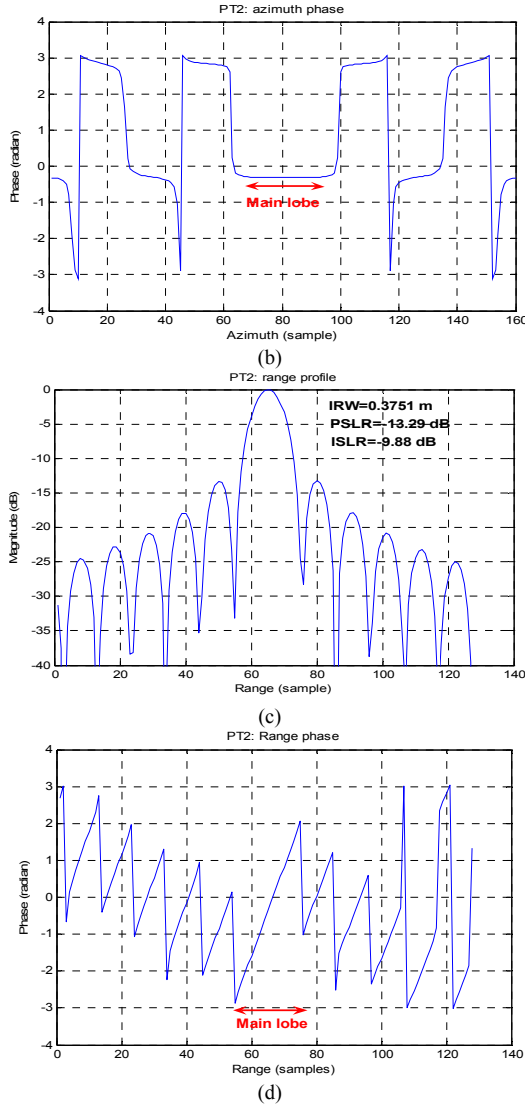


Fig. 9. Impulse responses and phases of PT2 after the compensation of residual phase. (a) Azimuth profile. (b) Azimuth phase. (c) Range profile. (d) Range phase.

V. PROCESSING RESULTS OF REAL BISTATIC SAR DATA

To validate the processing for the airborne/stationary bistatic SAR configuration, the algorithm is applied on real bistatic data. The data is collected in December 2007 by using FGAN's airborne SAR/GMTI system (PAMIR) acting as a moving receiver and a stationary transmitting antenna horn. In this bistatic SAR experiment, the receiver worked in the spotlight mode, shown in Fig. 3a. In this experiment, transmitter and receiver had an azimuth beam width of 27° and 6° , respectively. Both transmitter and receiver worked at X-band and shared a common bandwidth of 380MHz with a center frequency of 9.65 GHz. The effective composite exposure time in azimuth was 6s. The transmitter was located above the Rhine valley near the city of Bonn. The altitude difference between the illuminated scene center and the phase center of the horn antenna was only 100 m. In this experiment, because of complex flight condition, the airplane has a

nominal flight direction of 282.034° with a yaw angle of 286.24° in the North-East-Up coordinate system [21]. It means that the experiment is performed in low squint mode with a squint angle of 4.2° .

This experiment is also seen as a primary step for our further bistatic experiments using TerraSAR-X as the transmitter and PAMIR as the bistatic receiver [19]-[20].

Both local oscillators were not synchronized in this experiment. To mitigate the effects of the clock drift, we used two approaches. The first one was a larger echo window at the receiver side and the second one compensated the clock drift in the preprocessing.

By using the proposed imaging algorithm, the focused bistatic SAR image is shown in Fig. 10 (b). For comparison, the optical image of the processed scene and the bistatic SAR image processed by the time domain algorithm (i.e. the back projection algorithm [22]) are also shown in Fig. 10 (a) and Fig. 10 (c), respectively.

Because a stationary transmitter was used, the illumination pattern of the horn antenna becomes clearly visible. In addition, large shadows are present due to the small depression angle of the horn antenna (5°).

For further clarity of image quality, the part of scene centre (see the solid line) has been highlighted in more detail in Fig. 11. Comparing Fig. 11(b) and Fig. 11 (c), it can be found that the proposed algorithm nearly reaches the performance of the back projection algorithm.

VI. CONCLUSION

This paper discusses a bistatic SAR configuration (i.e. with a stationary transmitter and a moving receiver) and derives an accurate Bistatic Point Target Reference Spectrum by using the principle of stationary phase.

In comparison with bistatic SAR systems with two moving platforms, this point target reference spectrum contains a special range offset component introduced by the stationary platform. It is independent of the azimuth time variable, but dependent on the azimuth coordinate of a target. The key idea of the presented algorithm is to correct the CDRO along a hyperbola in the coarse image domain so that all targets having the same Doppler history are aligned in the same range bin. Subsequently, the proper azimuth compression is efficiently done in the frequency domain. To achieve this, the range blocking and interpolation are used. A simulation experiment and real raw data processing are performed to verify the accuracy of the presented algorithm.

However, the presented approach is only suitable in the specific case where the imaged scene has a small extension in azimuth where the CDRO is not significant. As the size of the composite scene in azimuth increases, the CDRO might spread over several range blocks along the range (see Appendix A). In this case, an additional blocking in azimuth is needed. By blocking in azimuth, we keep the maximum range offset difference in every azimuth block within a range block. Thus, this additional azimuth blocking will reduce the efficiency of this method.

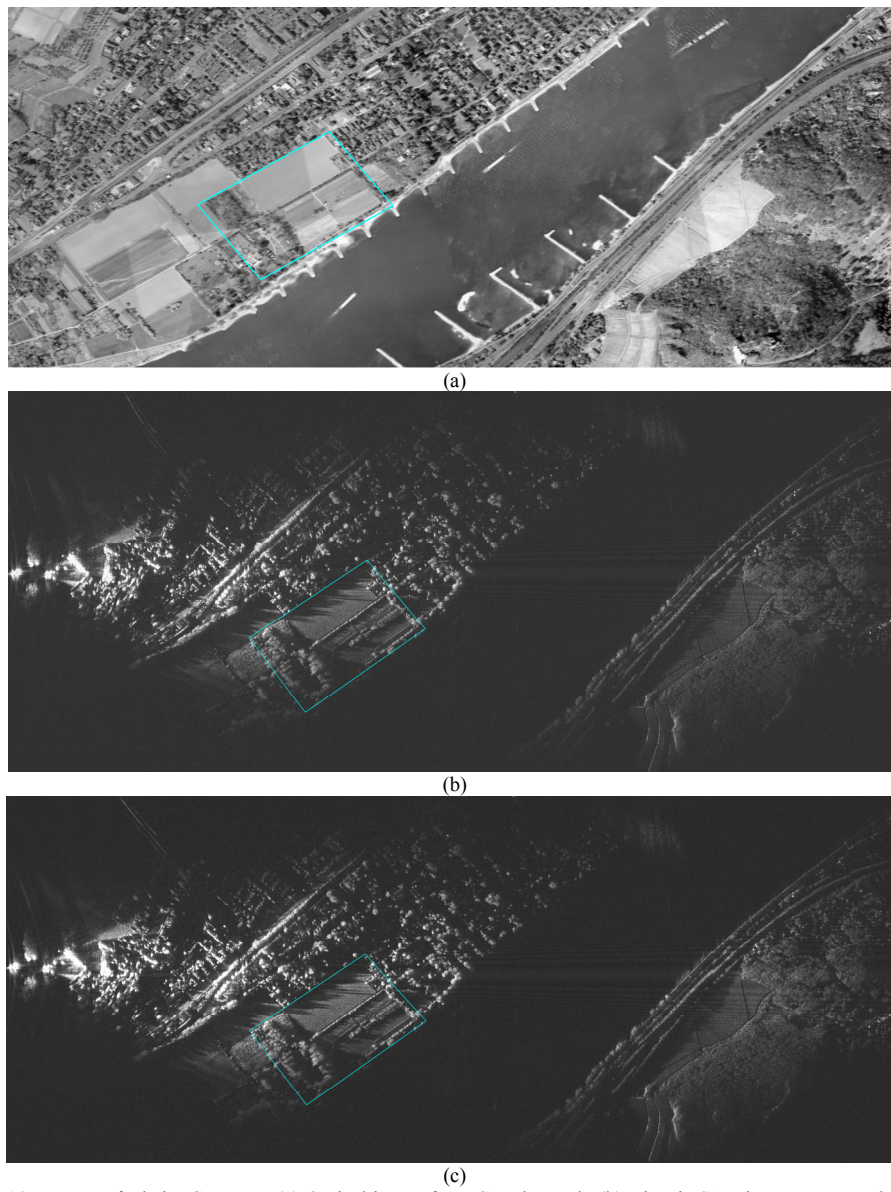
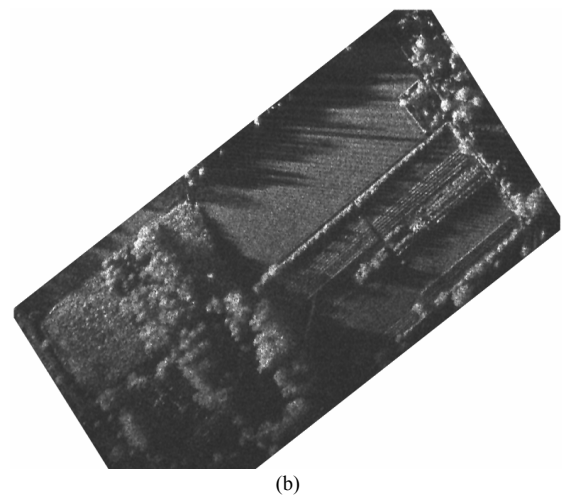
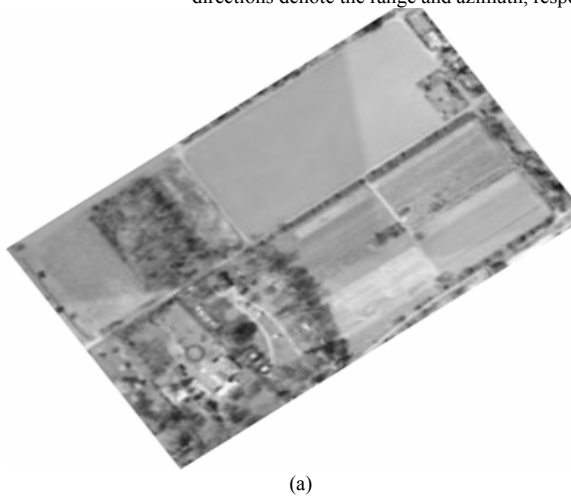


Fig. 10. Images of Rhein, Germany. (a) Optical image from Google Earth. (b) Bistatic SAR image processed by the presented algorithm. (c) Bistatic SAR image processed by the back projection algorithm. The horizontal and vertical directions denote the range and azimuth, respectively.



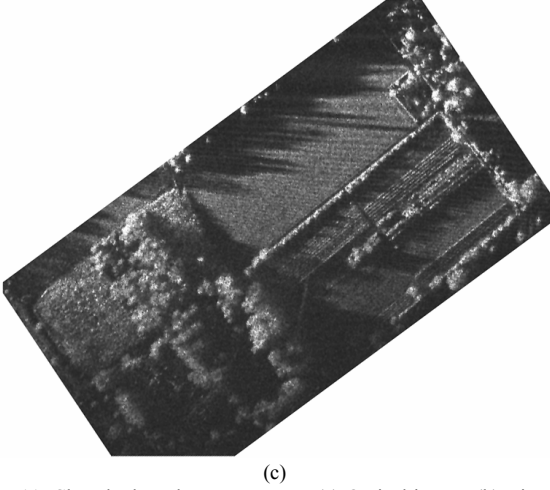


Fig. 11. Close look at the scene centre. (a) Optical image. (b) Bistatic SAR image processed by the proposed algorithm. (c) Bistatic SAR image processed by the back projection algorithm.

APPENDIX A (ANALYSIS OF BLOCK SIZE)

This appendix derives the block sizes in range and azimuth. The block size in range, ΔW_r , can be readily derived by using (19) and (11), and given as

$$\Delta W_r = \frac{\delta_r}{\max\left[\frac{1}{D} - 1\right]} \approx \delta_r \frac{8r_{0r}^2}{\left[L_e + (1 - \tilde{\kappa})L_s\right]^2} \quad (31)$$

The azimuth blocking is introduced to keep the maximum range offset difference, Δ_{ro} , in every azimuth block within a range block, i.e.

$$\Delta_{ro} \leq \Delta W_r \quad (32)$$

Let L_1 and L_2 be the azimuth offsets of the azimuth edges of one block from the scene center. The resulting azimuth block size can be expressed as

$$\Delta W_A = |L_1 - L_2| \quad (33)$$

At the azimuth edges, the range offsets, Δ_1 and Δ_2 , can be formulated by combining (3) and (25) as

$$\begin{aligned} \Delta_1 &= \sqrt{r_{0T\min}^2 + L_1^2} - r_{0T\min} \approx \frac{L_1^2}{2r_{0T\min}} \\ \Delta_2 &= \sqrt{r_{0T\min}^2 + L_2^2} - r_{0T\min} \approx \frac{L_2^2}{2r_{0T\min}} \end{aligned} \quad (34)$$

Where $r_{0T\min}$ denotes the nearest slant range variable r_{0T} in the block.

The maximum range offset difference in the block can be formulated by combining (33) and (34) as

$$\Delta_{ro} = |\Delta_1 - \Delta_2| = \frac{(L_1 + L_2)}{2r_{0T\min}} \Delta W_A \quad (35)$$

Substituting (31) and (35) into (32) yields

$$\Delta W_A \approx \min \left\{ \frac{16r_{0r}^2 r_{0T\min}}{\left[L_e + (1 - \tilde{\kappa})L_s\right]^2 (L_1 + L_2)} \delta_r \right\} \quad (36)$$

From (31) and (36), the block sizes in both directions are proportional to slant range variables, and inversely

proportional to the azimuth footprint length of transmitter and length of flight path of receiver. It means that the longer the length of the azimuth footprint of transmitter and length of flight path of receiver are, the more the azimuth blocks are needed, which will lead to inefficiency of this method.

ACKNOWLEDGMENT

This work reported herein is part of the joint DFG (German Science Foundation) research initiative Bistatic Exploration (PAK 59) of ZESS and FGAN, individually funded under grant numbers Lo 455/7-2, EN 731/1-2, and EN 731/3-2, which is gratefully acknowledged. The authors would furthermore like to point out the excellent and very effective cooperation between ZESS and FHR/FGAN, which is seen as a key item of their work. Finally the authors would like to thank the anonymous reviewers for their competent and helpful suggestions to improve this paper.

REFERENCES

- [1] J. H. Ender, I. Walterscheid, and A. Brenner, "New aspects of bistatic SAR: processing and experiments," in *Proc. IGARSS*, Alaska, USA, Sept. 2004, pp. 1758-1762.
- [2] O. Loffeld, H. Nies, V. Peters, and S. Knedlik, "Models and useful relations for bistatic SAR processing," *IEEE Trans. on Geosci. Remote Sens.*, vol. 42, no. 10, pp.2031-2038, Oct. 2004.
- [3] G. Krieger, and A. Moreira, "Spaceborne bi- and multistatic SAR: potential and challenges," *IET Radar Sonar Navig.*, vol. 153, no. 3, pp.184-198, Jun. 2006.
- [4] D. Mssonnet, "Capabilities and limitations of the interferometric cartwheel," *IEEE Trans. on Geosci. Remote Sens.*, vol. 39, no. 3, pp.506-520, Mar. 2002.
- [5] I. Walterscheid, J. H. G. Ender, J. Klare, A. R. Brenner, and O. Loffeld, "Bistatic image processing for a hybrid SAR experiment between TerraSAR-X and PAMIR," in *Proc. IGARSS*, Denver, Colorado, USA, Aug. 2006, pp. 1934-1937.
- [6] T. Espeter, I. Walterscheid, J. Klare, C. Gierull, A. R. Brenner, J. H. G. Ender, and O. Loffeld, "Progress of hybrid bistatic: synchronization experiments and first imaging result," in *Proc. EUSAR*, Friedrichshafen, Germany, June 2008.[CD-ROM].
- [7] I. G. Cumming and F. H. Wong, *Digital Processing of Synthetic Aperture Radar Data Algorithms and Implementation*. Norwood, MA: Artech House, 2005.
- [8] R. K. Raney "A new and fundamental Fourier transform pair. In *Proc. IGARSS*, Clear Lake, TX, May 1992, pp. 106-107.
- [9] Y. L. Neo, F. H. Wong, and I. G. Cumming, "A two-dimensional spectrum for bistatic SAR processing using series reversion," *IEEE Geosci. Remote Sens. Letters*, vol. 4, no.1, pp. 93-96, Jan. 2007.
- [10] F. H. Wong, and T. S. Yeo, "New applications of nonlinear chirp scaling in SAR data processing," *IEEE Trans. on Geosci. Remote Sens.*, vol. 39, no.5, pp. 946-953, May 2001.
- [11] J. Sanz-Marcos, P. Prats, J. J. Mallorqui, and A. Aguasca, "A subaperture range-Doppler processor for bistatic fixed-receiver SAR," in *Proc. EUSAR*, Dresden, Germany, May 2006.[CD-ROM]
- [12] I. C. Sikaneta, "A hybrid SAR processing method for data collected using a stationary bistatic receiver," in *Proc. EUSAR*, Friedrichshafen, Germany, June 2008.[CD-ROM].
- [13] J. H. G. Ender, "The double sliding spotlight mode for bistatic SAR," in *Proc. IRS*, Cologne, Germany, Sep. 2007, pp.329-333.
- [14] R. Lanari, S. Zoffoli, E. Sansosti, G. Fornaro, and F. Serafino, "New approach for hybrid strip-map/spotlight SAR data focusing," *IEE Proc. Radar, Sonar Navigation*, vol. 148, no. 6, pp.363-372, Dec. 2001.
- [15] D. P. Belcherand, and C. J. Baker, "High resolution processing of hybrid strip-map/spotlight mode SAR," *IEE Proc. Radar, Sonar & Navigation*, vol. 143, no. 6, pp.366-374, December 1996.

- [16] O. Loffeld, F. Schneider, and A. Hein "Focusing SAR images by inverse scaled Fourier transform," in *Proc. Int. Conf. Signal process. Commun.*, Las Palmas, Spain, 1998, vol.2, pp. 630-632.
- [17] B. R. Lanari, M. Tesaro, E. Sansosti, and G. Fornaro, "Spotlight SAR data focusing based on a two-step processing approach," *IEEE Trans. on Geosci. Remote Sens.*, vol. 39, no. 9, pp. 1993-2004, Sep. 2001.
- [18] J. Mittermayer, A. Moreira, and O. Loffeld, "Spotlight SAR data processing using the frequency scaling algorithm," *IEEE Trans. Geosci. Remote Sensing*, vol. 37, pp. 2198-2214, Sept. 1999.
- [19] R. Wang, O. Loffeld, Q. Ul-Ann, H. Nies, A. Medrano-Ortiz, and S. Knedlik, "A special point target reference spectrum for spaceborne/Airborne bistatic SAR processing," in *Proc. EUSAR*, Friedrichshafen, Germany, June 2008.[CD-ROM]
- [20] R. Wang, O. Loffeld, Q. Ul-Ann, H. Nies, A. Medrano-Ortiz, and S. Knedlik, "Analysis and extension of Loffeld's Bistatic Formula in spaceborne/Airborne configuration," in *Proc. EUSAR*, Friedrichshafen, Germany, June 2008.[CD-ROM]
- [21] B. Hofmann-Wellenhof, H. Lichtenegger, and J. Collins, *GPS: Theory and practice*. Wien: Springer Verlag, 2001.
- [22] M. D. Desai, and W. K. Jenkins, "Convolution back projection image reconstruction for spotlight mode synthetic aperture radar" *IEEE Trans. on Imag. Proc.*, vol. 1, no.4, pp. 505-517, Oct. 1992.



Robert Wang (M'07) received the B.S. degree in Control Engineering from the University of Henan, Kaifeng, China, in 2002, and the Dr. Eng. degree from the Graduate University of Chinese Academy of Sciences, Beijing, China, in 2007.

In 2007, he joined the Center for Sensorsystems (ZESS), the University of Siegen, Siegen, Germany. He is currently working at the hybrid bistatic experiment. He was also involved in some SAR projects for FGAN and DLR. His current research interests include monostatic and bistatic SAR signal processing, bistatic interferometric, airborne SAR

motion compensation, FMCW SAR system and Millimeter-wave SAR system.

Dr. Wang has contributed to invited sessions on bistatic SAR at EUSAR 2008 conference, and on understanding high resolution SAR images at European Radar Conference 2009. He is the coauthor of a tutorial entitled "Progress in bistatic SAR concepts & algorithms" presented at EUSAR 2008.



Otmar Loffeld (M'05-SM'06) received the Diploma degree in electrical engineering from the Technical University of Aachen in 1982, the Eng. Dr. degree, and the 'habilitation' in the field of digital signal processing and estimation theory in 1986, and 1989, respectively, both from the University of Siegen. He got the scientific research award of Northrhine-Westphalia ("Bennigsen-Foerder Preis") for his works on applying Kalman filters to phase estimation problems such as Doppler centroid estimation in SAR, phase and frequency

demodulation.

In 1991 he was appointed as a PROFESSOR for digital signal processing and estimation theory at the University of Siegen. Since then he gives lectures on General Communication Theory, Digital Signal Processing, Stochastic Models and Estimation Theory and Synthetic Aperture Radar. He is author of two textbooks on estimation theory.

In 1995 Prof. Dr. Loffeld became a member of the Center for Sensorsystems (ZESS) which is a central scientific research establishment at the University of Siegen (www.zess.uni-siegen.de). Since 2005 he is the Chairman of that Center.

In 1999 he became Principal Investigator (PI) on Baseline Estimation for the X-Band part of the Shuttle Radar Topography Mission (SRTM) where ZESS contributed to DLR's baseline calibration algorithms.

Prof. Loffeld is PI for interferometric techniques in the German TerraSAR-X mission, and, together with Prof. Ender from FGAN, he is one of the PI's for a bistatic spaceborne airborne experiment, where TerraSAR-X serves as the bistatic illuminator while FGAN's PAMIR system mounted on a Transall airplane is used as a bistatic receiver.

In 2002 he founded the International Postgraduate Programme (IPP) "Multi Sensorics", and, based on that programme, he established the "NRW Research

School on Multi Modal Sensor Systems for Environmental Exploration and Safety (MOSES) (www.moses-research.de) at the University of Siegen as an upgrade of excellence, in 2008. He is the speaker and coordinator of both doctoral degree programmes, hosted by ZESS. Furthermore is the university's scientific coordinator for "Multidimensional and Imaging Systems".

His current research interests comprise multi sensor data fusion, Kalman filtering techniques for data fusion, optimal filtering and process identification, SAR processing and simulation, SAR-interferometry, phase unwrapping, and baseline estimation. A recent field of interest is bistatic SAR processing.

Prof. Loffeld is a member of the ITG/VDE and Senior Member of the IEEE/GRSS.



Yew Lam Neo received the B.Eng. degree in electrical engineering from the National University of Singapore, Singapore, in 1994.

Dr. Neo was awarded the Engineering Book Prize and was the winner of the Innovation Prize Award for his final year project work on a VHF frequency synthesizer. He received his Ph.D. degree from the University of British Columbia, Vancouver, BC, Canada, in 2007. In 2006, he was a Visiting Scientist for three months with ZESS, University of Siegen, Siegen, Germany. He is currently continuing his

research in bistatic SAR signal processing.



Holger Nies received the Diploma degree in electrical engineering in 1999 and the Dr. Eng. degree in 2006, both from the University of Siegen.

Since 1999 he is a member of the Center for Sensorsystems (ZESS) at the University of Siegen and a lecturer in the Department of Signal Processing and Communication Theory.

He worked in the project sector "Optimal Signal Processing, Remote Sensing - SAR" of ZESS since 1999. He was also involved in some project work for Daimler AG (Stuttgart, Germany) in the field of

engine modeling and optimization. Currently he is working in the area of interferometric techniques in the German TerraSAR-X mission. He is Principal Investigator (PI) on the development of a stationary receiver SAR system for acquiring and processing signals transmitted from the TerraSAR-X satellite.

Dr. Nies received the "Best Poster Award" at EUSAR 2006 in Dresden, Germany. His current research interests include bistatic SAR processing, SAR interferometry and distributed data fusion.



Ingo Walterscheid (M'08) received the Diploma degree in electrical engineering and the Dr. Eng. degree from the University of Siegen, Siegen, Germany, in 2002 and 2007, respectively.

Since July 2002, he has been a Research Associate with the Research Institute for High Frequency Physics and Radar Techniques (FHR), Forschungsgesellschaft für Angewandte Naturwissenschaften (FGAN), Wachtberg, Germany. His current research interests are in the areas of bistatic SAR systems and experiments,

monostatic and bistatic SAR signal theory, and bistatic SAR processing.

Dr. Walterscheid is a member of the ITG/VDE. He received the IEEE Geoscience and Remote Sensing Society 2007 Transactions Prize Paper Award for a very significant contribution to the field of endeavor of the IEEE GRS Society.



Thomas Espeter (S'02-M'05) was born in Dülmen, Germany, in 1976. He received the Dipl.-Ing. degree in electrical engineering from Ruhr-Universität Bochum, Bochum, Germany, in 2005.

Since 2005, he has been with the Research Institute for High Frequency Physics and Radar Techniques (FHR), Forschungsgesellschaft für Angewandte Naturwissenschaften (FGAN), Wachtberg, Germany, as a Research Assistant. His current research interests are in the area of mono- and bistatic synthetic aperture radar.



Jens Klare (M'08) received the Diploma degree in physics from the Ruprecht-Karls-Universität Heidelberg, Heidelberg, Germany, in 1998 and carried out his diploma thesis at the Max-Planck-Institute for Astronomy in Heidelberg, Germany. He received the Ph.D. degree in astronomy from the Rheinische Friedrich-Wilhelms-Universität Bonn, Bonn, Germany, in 2003. He performed his Ph.D. thesis at the Max-Planck-Institute for Radio Astronomy in Bonn, Germany with the investigation of active galactic nuclei, supermassive binary black hole systems, and ultra-relativistic plasma jets using Very Long Baseline Interferometry (VLBI) at highest frequencies and space-VLBI at longest baselines. From 2003 to 2004 he was a postdoctoral research fellow at the Max-Planck-Institute for Radio Astronomy in Bonn, Germany.

In 2004, he joined the Institute for High Frequency Physics and Radar Techniques (FHR) of the Research Establishment for Applied Science (FGAN), Wachtberg, Germany. His current research interests include array-based radar imaging, signal processing of MIMO radar systems, 3D-SAR, bi- and multistatic SAR, and digital beamforming.

Dr. Klare is a member of EuMA and DPG.



Joachim H. G. Ender (M'02-SM'06) received the diploma degree in mathematics and physics from the Westphalian Wilhelm University of Münster, Germany in 1975 and the Ph.D. degree in electrical engineering from Ruhr-University Bochum, Germany.

In 1976 he was with the Research Establishment of Applied Science (FGAN), Wachtberg, Germany. Since 1992 he has been giving annual lectures on radar signal processing at the Ruhr-University Bochum, which conferred the title Honorary

Professor upon him in 2002. He also gives lectures on radar techniques at the Rhineish-Westphalian Technical-University, Aachen, Germany and the University of Siegen, Germany. In 1999, he was the head of the Electronics Department, Research Institute for High Frequency Physics and Radar Techniques (FHR), FGAN, where he initiated and supervised research activities for various aspects of phased array and imaging radars, including the design and operation of experimental SAR systems, such as AER-II and PAMIR. Since 2003, he has been the director of FHR, and he was elected Vice Chairman of the FGAN in August 2007. He is executive board member of the German Institute of Navigation as well as Member-at-Large of North Atlantic Treaty Organization Sensors and Electronics Technology research panel. He further acts as Review Board Member of the German Research Foundation and as a Review Board Member of the Leibniz Society. His current research interests are very high resolution SAR imaging, 3D-SAR, MIMO-SAR, multibaseline and wideband processing techniques for across-track SAR interferometry, ground moving target indication with air and space-based radar including multistatic satellite constellations, inverse SAR for moving target imaging and bistatic SAR processing. He authored and coauthored numerous papers in various international journals and conferences.

Dr. Ender, jointly with colleagues, received the German Society for Information Technology Paper Prize Award of the Association of German Electrical Engineers in 1992 and the IEEE-TRANSACTIONS ON GEOSCIENCE AND REMOTE SENSING Best paper award in 2006. In 1996, he was one of the founding members of the biannual "European Conference on Synthetic Aperture Radar".